Lab on a Chip

PAPER

View Article Online
View Journal

Cite this: DOI: 10.1039/d6lc00107f

3D printing monolithic, multifunctional polymer acoustofluidic devices with tunable mixing and particle focusing

Roxanne Kate Balanay, †[a] Justin W. Yip,†[a] Justin Do,[a] Omair Adil,[a] Keith Johnson[a] and Tyler R. Ray *[ab]

Acoustic forces offer a powerful, contact-free modality for manipulating particles and fluids within microfluidic lab-on-a-chip systems. However, realizing the full potential of acoustic manipulation has been constrained by conventional cleanroom-based fabrication methods. Typically formed from high-acoustic-impedance materials like silicon or glass, these processes yield devices with limited design complexity owing to the planar channel geometries inherent in micromachining. Here, we introduce a class of polymer-based acoustofluidic platforms fabricated using micro-digital light processing (μDLP) 3D printing. In contrast to micromachining, this additive manufacturing approach enables complex, truly three-dimensional (3D) microfluidic architectures in a monolithic device form factor. We demonstrate strategies to overcome challenges associated with low-acoustic-impedance polymer resins and establish design rules based on precise control over channel and surrounding material dimensions (*e.g.*, wall thicknesses) to achieve robust acoustofluidic functions including efficient sharp-edge-based mixing and effective particle focusing using a bulk acoustic wave resonance mode. By leveraging the design freedom provided by additive manufacturing, we fabricated an integrated, monolithic device driven by a single piezoelectric element that sequentially performs acoustic mixing and focusing within spatially distinct regions enabled by engineered variations in the 3D channel structure. This work establishes μDLP additive manufacturing as a key enabler for next generation acoustofluidic platforms by demonstrating how true 3D architectural control over channel geometry can yield integrated, multifunctional polymer acoustofluidic devices with an expanded functional design space.

Received 5th February 2026,
Accepted 19th February 2026

DOI: 10.1039/d6lc00107f

rsc.li/loc

Introduction

Controlled spatial manipulation of microscale constituents in fluid represents one of the key defining challenges in developing lab-on-chip technologies. Magnetic, electrokinetic, and optical approaches offer powerful strategies for achieving precision spatial control over targets of interest such as biological cells or magnetic beads; however, limitations resulting from throughput, biocompatibility, and fabrication considerations can hinder utility of such control strategies within a microfluidic lab-on-chip platform. In this context, acoustic forces represent an attractive alternative force handle and garner significant interest[1–3] as a means of achieving spatiotemporal control over both suspended matter (*e.g.*, particles, cells, organoids) and complex fluid flows. Such acoustofluidic platforms[4,5] are relatively material agnostic[6,7] as the interaction of acoustic forces depends upon intrinsic material properties rather than extrinsic labeling or material-specific parameters (*e.g.*, magnetism). As acoustic forces can control matter across multiple length scales, recent examples highlight use in high-throughput cell sorting,[5,8–10] drug delivery,[11–13] and the directed material assembly.[6,14–17] In aggregate, the unique advantages of acoustofluidic platforms offer powerful capabilities in a diverse array of applications spanning point-of-care diagnostics[5,18] to advanced manufacturing.[6,14,19–21]

Acoustofluidic devices leverage both acoustic streaming and acoustic radiation forces to enable both solution mixing and particle positioning (Fig. 1). Acoustic streaming[22,23] drives bulk fluid motion to enhance mixing[24–28] and is typically classified as either boundary layer streaming along solid surfaces, Eckart streaming in high-frequency regimes, or cavitation microstreaming from oscillating bubbles.[22] Sharp-edge oscillator[22,29] microfluidics leverage boundary layer streaming to induce efficient mixing (Fig. 1C) and are thus the predominate design utilized in acoustofluidic micromixing devices.

[a] *Mechanical Engineering, University of Hawai'i at Manōa, Honolulu, Hawaii, USA. E-mail: raytyler@hawaii.edu*
[b] *Cell and Molecular Biology, John A. Burns School of Medicine, University of Hawai'i at Manōa, Honolulu, HI 96822, USA*
† These authors contributed equally.

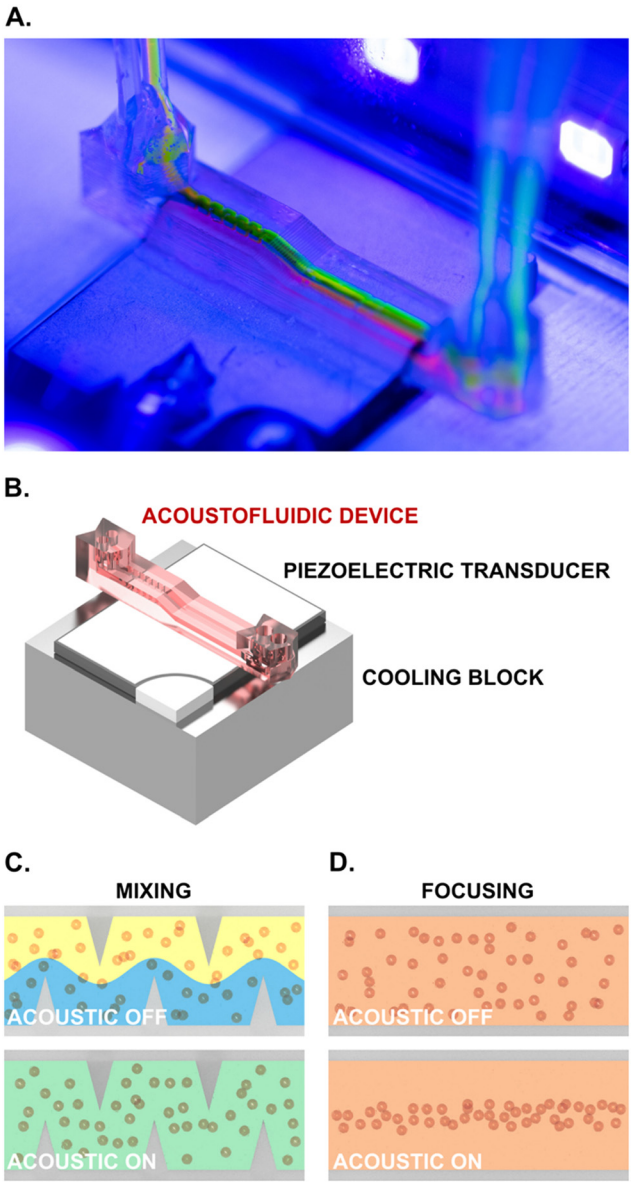

Fig. 1 (A) Photograph of the experimental setup under UV light and (B) schematic illustration showing a resin 3D-printed chip adhered to a piezoelectric transducer, which is coupled to a cooling block to dissipate heat generated during acoustic application. Schematic of fluid and particle distribution on a (C) mixing and (D) focusing platform.

In a complementary manner, acoustic radiation forces direct particle motion (acoustophoresis) through the acoustic contrast between the suspended particles and the surrounding fluid.[6,15,21] Standing waves of pressure generated by piezoelectric actuators resonating the propagation medium drive particles either toward or away from pressure nodes as a consequence of the density and compressibility mismatches between the focusing target and surrounding media (Fig. 1D). A one-dimensional model[10,30–32] (eqn (1)) describes the acoustic radiation force F_{rad} acting on particles.

$$F_{rad} = -\frac{\pi P_1^{\,2} V_p \beta_f}{2\lambda}\phi(\beta,\rho)\sin(2kx) \quad (1)$$

Here, P_1 is the applied acoustic pressure amplitude, V_p is the particle volume, β_f is the compressibility of the fluid, λ is the wavelength, $\phi(\beta, \rho)$ is the acoustic contrast factor, k is the wave number, and x is the particle position. By varying the applied peak-to-peak voltage, one can linearly increase the pressure amplitude P_1 to increase the strength of the applied acoustic force.[10,33] As the force scales with particle volume, larger particles experience stronger focusing effects.[10] The acoustic contrast factor (eqn (2)), defined as the ratio of particle compressibility and density to the surrounding medium, determines the direction of particle movement.

$$\phi = \frac{5\rho_p - 2\rho_f}{2\rho_p + \rho_f} - \frac{\beta_p}{\beta_f} \quad (2)$$

Here, β_f is the compressibility of the surrounding fluid, β_p is the compressibility of the particles, ρ_f is the density of the surrounding fluid medium, ρ_p is the density of the particles. Particles with a positive acoustic contrast factor (*e.g.*, high density; low compressibility compared to surrounding medium) move towards the pressure node, while those with a negative contrast factor move towards the antinode.[30,34,35]

The two principal strategies for acoustic wave propagation in acoustofluidic devices are surface acoustic waves (SAW) and bulk acoustic waves (BAW). BAW systems commonly employ piezoelectric elements to establish standing waves of pressure in configurations comprising either pairs piezoelectric elements or through a single element coupled with a high-impedance reflector.[5] Fabrication of conventional BAW-based acoustofluidic devices[36,37] requires use of cleanroom-based environments and capital-intensive processes (*e.g.*, photolithography, deep-reactive silicon etching – DRIE) to form microfluidic channel geometries in silicon.[38,39] Alternative fabrication approaches seek to utilize mass-manufactured glass capillaries[40–42] or polymeric materials;[43,44] however, such approaches introduce new limitations including restricted design geometries (*i.e.* glass capillaries) or reduced performance capabilities. For the approaches utilizing polymers such as polydimethylsiloxane (PDMS) and poly(methyl methacrylate) (PMMA) the lower acoustic impedance of the polymer materials results in a decreased efficacy for reflecting standing waves yielding resonance behavior that differs from platforms utilizing high-impedance materials.[43,45,46] Thus, while these initial demonstrations highlight significant potential for polymeric acoustofluidic devices, the limited number of studies highlight the need for establishing a new set of device design parameters to expand broad utilization.

Additive manufacturing, especially stereolithography (SLA) and digital light processing (DLP), holds immense promise for overcoming constraints encountered in traditional microfabrication of acoustofluidic devices or use of polymeric materials by enabling production of devices with true three-dimensional (3D) microfluidic architectures. Although current 3D-printing resolutions can lag behind those achievable in cleanroom processes, these techniques uniquely permit

complex device geometries that are otherwise challenging or impossible to realize.[47,48] Such geometries can support more effective acoustophoretic device performance.[49] Recent demonstrations of 3D-printed acoustofluidic devices, for example, highlight early successes in particle separation,[50] yet many open questions remain regarding the interplay between material properties, channel geometries, and acoustic wave propagation in low-impedance resins.

In this work, we introduce a new class of 3D-printed acoustofluidic platforms that combine micromixing and particle focusing functionalities in a single, integrated device. By drawing upon design principles from established sharp-edge micromixers fabricated *via* soft lithography,[26,27] we develop an acoustically driven micromixer with well-defined sharp-edge features and demonstrate its robust performance in efficiently mixing fluids across a range of flow conditions. We further present a complementary particle-focusing module, validated in two distinct media, to illustrate the broad applicability of these 3D-printed systems in manipulating suspended matter. Finally, in a multilayer design, we unite these capabilities to highlight how 3D printing enables complex, multifunctional geometries that were previously challenging or impossible to realize using conventional microfabrication strategies. Collectively, these findings establish a blueprint for leveraging emerging additive manufacturing approaches to expand the design space, streamline fabrication, and enhance the functionality of next-generation acoustofluidic devices.

Materials and methods

Device fabrication

A micro digital light processing (μDLP) resin printer (MiiCraft Profluidics 285D, Creative CADworks) fabricated all acoustofluidic devices from resin formulated for microfluidic applications (MiiCraft BV-007A, Creative CADworks) with a layer thickness of 50 μm. Subsequent removal of fabricated devices at the conclusion of the printing process facilitated a post-processing sequence. After a brief isopropyl alcohol (IPA) submersion (~10 s), flushing of internal printed features (*e.g.*, channels) with deionized (DI) water, sonication in DI water for 4 min, drying by compressed air, UV-curing (5 min, CureZone, MiiCraft), and oven-based heat treatment (15 min, 70 °C) produced finished acoustofluidic devices.

Acoustophoretic experiments

A custom-built experimental system comprising a function generator (SDG 2042X, SIGLENT), a power supply (1673, B&K Precision), an amplifier (LZY-22+, Mini Circuit), and a piezoelectric element (SMPL20W15T21R111, STEMiNC) generated prescribed acoustic fields within the 3D-printed acoustofluidic devices. Unless otherwise noted, experiments utilized a 1 MHz frequency at a peak-to-peak voltage (V_{pp}) of 45 V_{pp} to generate prescribed acoustic fields in the acoustofluidic devices.

3D-printed acoustofluidic devices were bonded onto piezoelectric transducers using adhesive (Super Glue Micro Precise Gel, Gorilla and 6-621-GEL, Dymax). Thermally conductive transfer tape (8810, 3M) then secured each chip-transducer unit to a cooling block, thereby minimizing temperature-related drift in the piezoelectric response. A USB camera (GS3-U3-51S5C-C, FLIR) interfaced with a stereo microscope (SPZ-50, Aven) provided real-time visualization. Control of the acoustic input parameters—frequency, voltage, and pulse duration—was implemented *via* a custom MATLAB-based graphical user interface.

For fluorescent imaging of micromixing, a UV light source (10 W Blacklight Strip Lights, Barrina) illuminated a 0.5 w/w% fluorescein sodium salt solution (46960, Sigma-Aldrich). A thin Kapton film (1 mil) placed over the objective lens blocked observation of a co-flowing, non-fluorescent, blue-dyed water (Soft Gel Paste, AmeriColor) by allowing transmission of only the fluorescence signal into the objective. In studies investigating acoustic focusing (alone) or the combined acoustic mixing/focusing configuration, both the UV illumination and Kapton filter were removed in favor of brightfield microscopy *via* the internal microscope illumination source. Prescribed microfluidic flow was provided *via* either a single-syringe pump (Pump 11 Elite Single Syringe, Harvard Apparatus) or a dual-syringe system (4002X, New Era) with selection depending on the requirements of each experiment.

Six distinct fluid mixtures were prepared for demonstration acoustofluidic experiments. Unless otherwise noted, all aqueous solutions and electrolytes were prepared with deionized (DI) water Millipore (resistivity 18.25 MΩ cm^{-1}, Milli-Q, Millipore). (1) A 0.5 w/w% fluorescein sodium salt (46960, Sigma-Aldrich) solution; (2) A 0.6 w/w% visible blue dye (Soft Gel Paste, AmeriColor) tracer solution; (3) 2 w/w% black paramagnetic polyethylene microspheres (BKPMS-1.2, 38–45 μm, Cospheric) suspended in silicone oil (378380, Sigma-Aldrich), which we refer to as BPPM-SI; (4) 0.5 w/w% orange fluorescent polymer microspheres (FMO-1.3, 1–5 μm, Cospheric) suspended in (1) 0.5 w/w% fluorescein sodium salt solution (noted as OFPM-FSS); (5) 0.04 mg mL^{-1} streptavidin magnetic beads (MB-STRP) (Pierce™ Streptavidin Magnetic Beads, Thermo Scientific™); (6) 0.02 mg mL^{-1} biotinylated peroxidase (Biotin-HRP) (Invitrogen™). (5) and (6) are both prepared in 10 mM, pH 7.4 phosphate-buffered saline (PBS) (MP Biomedicals™) containing Tween-20 (Sigma-Aldrich) (PBS : Tween-20 volume ratio 100 : 0.05).

Calculation of mixing index

The mixing index (MI)[51,52] quantifies mixing performance from 0 (unmixed) to 1 (fully mixed), with 0.9 as the threshold for acceptable mixing. A MATLAB script calculates MI from acquired images. Here, a mask of the channel inclusive of spike features overlaid on the image of interest covers the device top and bottom to exclude edge effects when evaluating pixel intensities (Fig. S1E). This masking isolates the channel's interior (no edge, no spike), ensuring only valid data is analyzed. MI is then calculated for each column along the device length across all acquired images throughout the experiment.

UV-vis analysis

100 μL of the acquired mixture of MB-STRP and Biotin-HRP from the acoustic off and acoustic on conditions were washed three times with PBS using a DynaMag magnet (DynaMag™-2 Magnet, Invitrogen™). Subsequently, 150 μL of 3,3′,5,5′-tetramethylbenzidine (TMB) (1-Step™ TMB ELISA Substrate Solution, Thermo Scientific™) was added to the magnetically separated complex, resulting in the development of a blue color. Afterward, 200 μL of 2.5 M sulfuric acid (ACS reagent, 95.0–98.0%, Sigma-Aldrich) was added as a stop solution, causing the solution to turn yellow. The solution was decanted with the help of a DynaMag magnet and characterized using a UV-visible spectrometer (Ocean High-Resolution Spectrometer, Ocean Optics).

Results and discussion

3D-printed acoustofluidics: acoustic mixing

A 3D-printed Y-channel micromixer (Fig. 2A) incorporates a series of sharp-edge spike features (Fig. 2B) to promote rapid fluid mixing. Sharp-edge spike features are commonly used in micromixer devices,[22,29] where acoustic excitation from a piezoelectric actuator induces tip vibrations that generate strong acoustic streaming with two counter-rotating vortices at each spike tip.[53] This approach leverages a well-known capability to enhance mixing efficiency through modifications to the spike geometry, as decreasing the tip angle can enhance mixing.[28,54] Moreover, configuring sharp edges in a staggered pattern, rather than in directly opposing positions, provides additional improvements in mixing performance.[54] In polymer acoustophoresis platforms the resonance phenomena occur across the entire device[55,56] which results in all dimensional features (*e.g.*, top and bottom walls, sidewalls, and channel cross-sections) holding the potential to critically influence acoustic wave propagation and resonance conditions.[56]

This design utilizes a nominal spike height of 350 μm, angle of 30°, and a staggered spacing of 750 μm, which yields 20 uniformly distributed spikes in total. Two visually distinct fluids—a blue tracer solution and a fluorescein solution—co-flow at rates of 3, 6, or 9 μL min^{-1} to assess device mixing performance. The mixing index (MI)[51,52] value quantifies the extent of mixing from the standard deviation of the pixel intensity (normalized) for a vertical range of pixels corresponding to the channel width. Values range from 0 (unmixed) to 1 (fully mixed), with 0.9 accepted[51,52] as the threshold for identifying a fully-mixed solution. The acoustofluidic channel designs ensure that purely diffusive mixing is insufficient to achieve MI ≥ 0.9.

Calculation of MI at the midpoint between spikes 10 and 11 (Fig. 2C) enable evaluation of the role of acoustics in promoting mixing. In the absence of acoustic excitation (initial 5 s), the MI follows the expected behavior that the degree of diffusive mixing is inversely proportional to flow rate (*e.g.*, slower flow rates exhibit higher calculated MI values resulting from diffusion). Immediately upon application of the acoustic field (t = 5 s) the value of MI increases in a stepwise fashion to initially surpass the 0.9 threshold before stabilizing under steady-state conditions. This results from the sharp-edge tips responding to the acoustic field to induce localized, accelerated channel mixing.[25,57]

Examining MI at spike positions across the channel length (Fig. 2D; additional flow rates shown in Fig. S1A and B) offers further insight into the interplay of diffusion and acoustic-driven mixing. In the absence of acoustic mixing, the MI value gradually increases with each progressive spike, reflecting cumulative diffusive mixing (as is expected). Immediately following the application of the acoustic field, the MI value increases abruptly and remains at or above 0.9. This performance underscores and confirms the robust capacity for acoustophoretic forces to promote mixing in microfluidic channels. While the 20 spike design is sufficient for the selected flow rates, expanding the number of sharp edges and fabricating sharper tips would likely yield even higher mixing performance for systems demanding higher flow rates or shorter channel lengths. This is a key advantage of the demonstrated efficacy of the 3D-printed device platform reported here as the design cycle to generate a device from optimized channel geometries is rapid as compared to conventional glass/silicon acoustophoretic device platforms (ranges from hours to days).

Representative microsopy images (Fig. 2E) provide insight into the influence of diffusive mixing (no field applied, t = 2 s), the flow behavior following the application of the acoustic field (t = 6 s), and steady-state operation (t = 18 s). In the absence of an applied acoustic field, the blue tracer and fluorescein solutions show diffusive mixing. Visible perturbations appear immediately following field application and by t = 18 s a uniform steady-state condition is established across the channel length.

Examining the dynamic changes in MI values as a function of time and channel position (Fig. 2F) offers additional insight to the performance of acoustophoretic mixing in a 3D printed device. Before field application, the influence of diffusive mixing is evident in the gradual increase in MI values as a function of channel length (*i.e.* transition from dark to light purple). Upon field application (t = 5 s) a sharp increase in MI values occurs across the channel length, which preceeds the transitory period in which the flow and acoustic fields stabilize. We note the observed fluctuations in MI during this transient likely reflect moment-to-moment variation in the local ratio of fluorescent to non-fluorescent fluid as the two streams interact *via* acoustic mixing. The waterfall plot in Fig. 2F highlights that once the system reaches steady state the MI values consistently remain above 0.9, indicating robust and sustained mixing throughout the microfluidic channel.

3D-printed acoustofluidics: acoustic focusing

Demonstrations of acoustically mediated particle focusing in 3D-printed devices underscore the critical interplay between material properties and structural design. In low-acoustic-

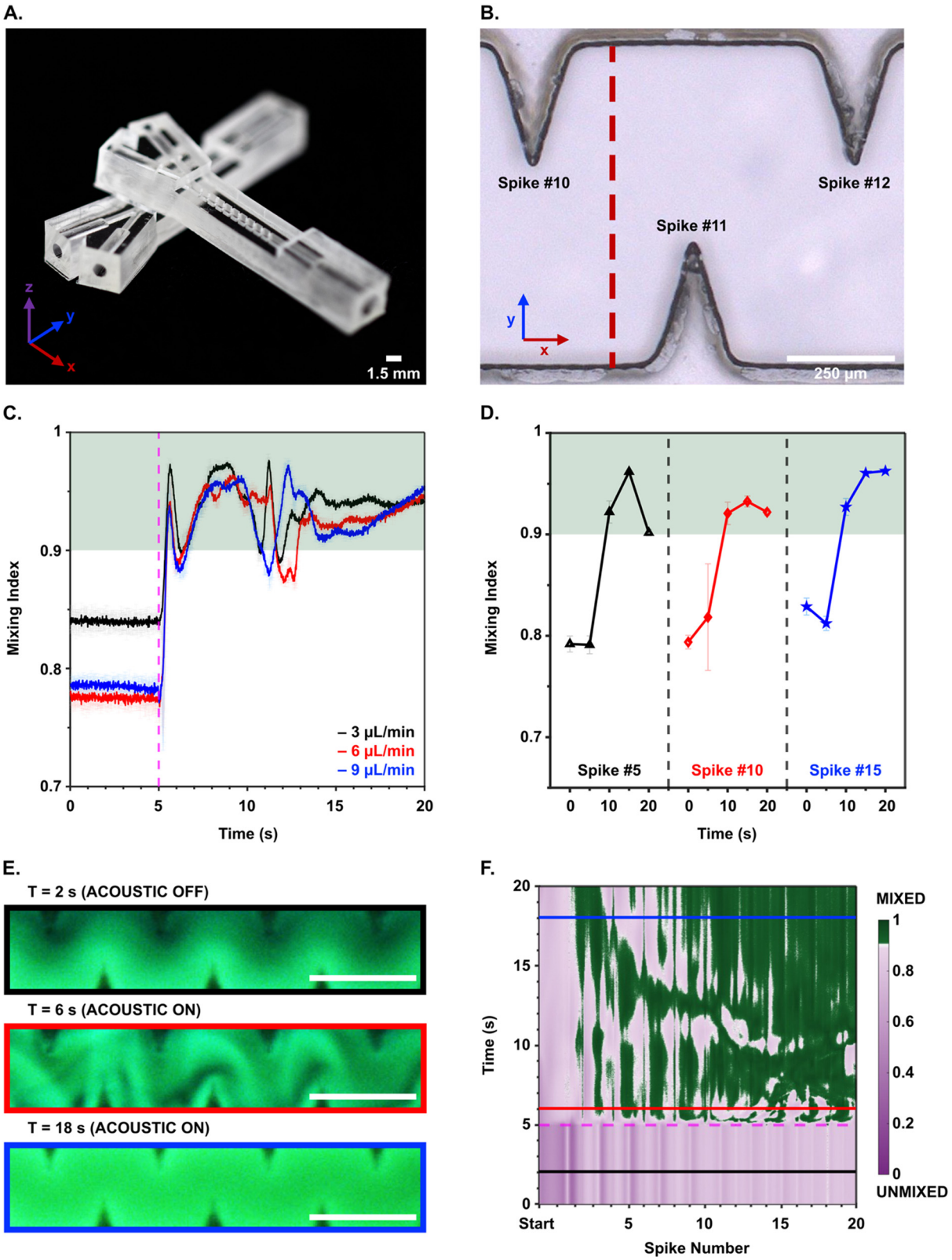

Fig. 2 (A) Photograph of a resin 3D-printed micromixer featuring spikes within the channel. (B) Schematic of the channel interior showing staggered spikes with numbering. The dark red dashed line indicates the analysis location at the midpoint between the spikes. (C) Mixing index (MI) at three flow rates (3, 6, and 9 μL min^{-1}) measured between spikes 10 and 11. All three flow rates achieved the considered mixing threshold. (D) MI at 9 μL min^{-1} across spike number during experimental acquisition. All spikes exceeded the considered mixing threshold when acoustic was enabled. (E) Representative images of micromixer at different time. Scale bars represent 750 μm. (F) MI at 9 μL min^{-1} in the region of interest over time. The magenta dashed line indicates the moment acoustic was enabled, while black, red, and blue solid lines represent images extracted in (E). As the spike number increases, mixing improves.

impedance materials, such as the polymeric resins utilized in vat photopolymerization 3D printing, single-transducer bulk acoustic wave (BAW) configurations can suffer from inadequate sound reflection, impeding the formation of a central pressure node.[58] Strategic optimizations to the device geometry,[43] such as the top (t_{top}) and bottom (t_{bottom}) dimensions (*e.g.*, device thickness) can enable robust wave reflection and thus effective particle focusing.

An acoustofluidic device (Fig. 3A) designed specifically for use at 1 MHz with a silicone oil-based medium (BPPM-SI) serves as an initial proof-of-concept. Internal microfluidic channel dimensions follow calculations for the resonant conditions to establish a half-standing wave (*i.e.*, one focusing node):

$$f = \frac{v_w}{\lambda} \quad (3)$$

$$\lambda = 2W \quad (4)$$

where f is the frequency, v_w is the speed of sound in the medium, λ is the wavelength in that medium, and W is the device channel width. The system parameters (f = 1 MHz, $v_{w,\ silicone\ oil}$ = 1040 m s^{-1}) result in a calculated channel width of 500 μm. A systematic investigation of the influence of t_{top} and t_{bottom} dimensions (Fig. 3B and S2) on focusing performance establish a 600 μm top channel thickness paired with a 400 μm bottom channel thickness supports a wave reflection condition that enables

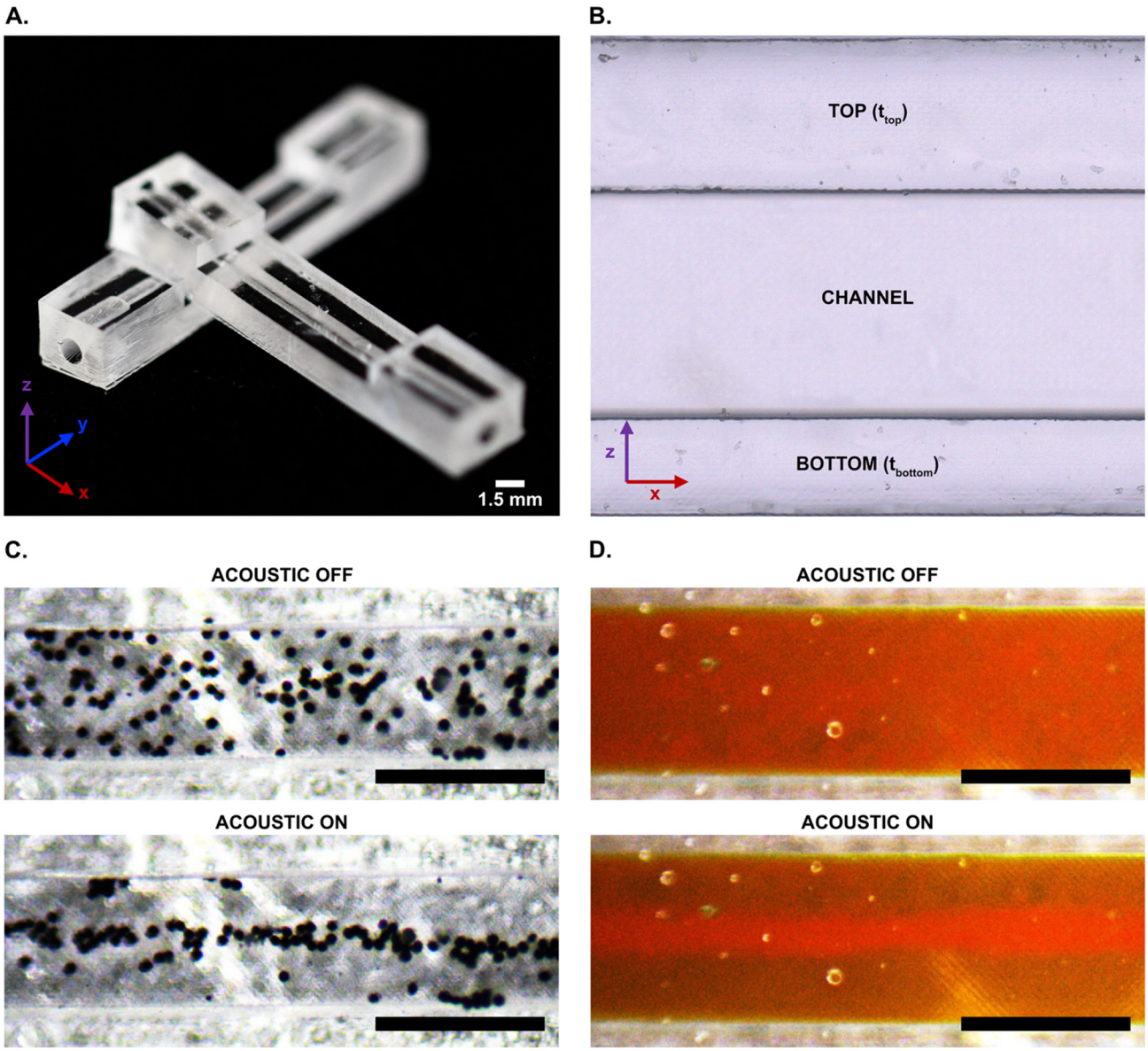

Fig. 3 (A) Photograph of a resin 3D-printed focusing device with a straight channel. (B) Side-view schematic of the device, showing varying thicknesses of the bottom (t_{bottom}) and top (t_{top}). (C) Black polyethylene microspheres suspended in silicone oil, imaged with acoustics off and on. Scale bars represent 750 μm. (D) Orange fluorescent polymer microspheres suspended in fluorescein salt solution, imaged with acoustics off and on. Scale bars represent 750 μm. In both cases, the microspheres aggregated at the channel center under acoustic conditions.

reliable particle focusing. This geometry optimization highlights the critical role of external channel dimensions (*e.g.*, material thicknesses) in achieving optimal performance in resin 3D-printed acoustic focusing devices.

These insights enable fabrication of two prototype device designs: (i) a 500 μm internal square channel for the BPPM-SI system and (ii) a 750 μm internal square channel for a water-based medium containing fluorescent particles (OFPM-FSS). Both devices share a uniform sidewall thickness of 1500 μm. Owing to the difference in the speed of sound for the two media (*i.e.*, silicone oil, water), the internal channel dimensions of each device ensure formation of a half-standing wave at 1 MHz to focus particles to the center node of the channel.

In the initial demonstration system utilizing BPPM-SI (Fig. 3C), a random dispersion of microspheres exists in the absence of an applied acoustic field. An immediate migration of the microspheres into the central pressure node occurs upon the application of the acoustic field. A similar phenomenon occurs in OFPM-FSS (Fig. 3D) system. Although the size and concentration of the particles in solution is below the threshold of visual observation for the microscopy system utilized in this work, the application of the acoustic field focuses the particles to the central pressure node resulting in the formation of a visible streamline of highly concentrated (and thus visible) particles.

These findings illustrate the importance of precisely engineering the channel dimensions and wall thickness in resin-based 3D-printed acoustofluidic devices to surmount the intrinsic limitations imposed by the use of low-acoustic-impedance materials. By deliberately optimizing the reflection conditions *via* dimensional tuning to produce a stable pressure node, single-line focusing can be reliably achieved. This consideration is in contrast to common approach to glass/silicon acoustofluidic device design space considerations owing to the ease at which focusing conditions can be established.

The native lateral (*XY*) resolution of a given μDLP printer is an additional consideration (in this work this is 40 μm *XY*, 5–500 μm *Z*-thickness) as it constrains both the minimum achievable feature size and the overall fidelity to a given geometry, particularly for narrow channels and sharp or delicate acoustic structures, relative to conventional microfabrication methods (*i.e.* soft lithography *via* cleanroom-fabricated molds). This fabrication process also restricts the materials library to photocurable polymeric systems (*i.e.* resins) resulting in devices that possess a low acoustic impedance. Thus, while fabrication of fine features is possible within these resolution limits, thin structures demonstrate increased susceptibility to damage during post processing. This is the result of the parts remaining mechanically fragile until fully cured. While this process is highly repeatable when utilizing identical materials, printer settings, and processing conditions, printed dimensions may deviate from nominal CAD dimensions. This is particularly notable in the bottom layers (*i.e.* those closest to the buildplate) due to compression effects that necessitate the use of a compensation factor to achieve a target thickness. This factor may vary with build-plate tolerances. Such variation may be minimized by utilizing a single build plate. As print performance can change over time, periodic characterization/calibration of both the printer and workflow is essential.

3D-printing expands the design space for acoustofluidics: an integrated, single piezo device

Validating that resin-based 3D-printed microfluidic chips can independently achieve both acoustic mixing and focusing unlocks an expansive microfluidic design space for acoustofluidic devices. Harnessing the inherent design freedom of additive manufacturing to realize fully three-dimensional fluidic structures, we demonstrate a unique single-piezoelectric-element acoustofluidic device that merges both functionalities of mixing and focusing (Fig. 4A). This system comprises three consecutive, independent regions: (i) a mixing region, (ii) a transition stage, and (iii) a focusing region (Fig. 4B and C).

Key to device operation is a 750 μm-wide internal channel sized to support the half-standing wave required for focusing a mixture of OFPM-FSS and blue-dyed tracer solution. The t_{top} and sidewall thicknesses remain constant at 600 μm and 1500 μm, respectively, while the t_{bottom} thickness transitions from 1150 μm in the mixing region to 400 μm in the focusing region. This purposeful geometric modulation prevents unintended particle focusing within the mixing stage, even in the presence of sharp-edge spikes. Instead, a smoothly tapered transition region gradually reduces the base thickness to ensure continuous flow and intended device behavior.

In the absence of acoustic excitation, a clear boundary persists between the two co-flowing fluids in the mixing zone (Fig. 4D and E; "ACOUSTIC OFF") observing only moderate diffusive mixing. Diffusive mixing progresses along the length of the channel (Fig. 4D and F; "ACOUSTIC OFF"), although the microspheres remain optically undetectable given the size and concentration. Upon application of the acoustic field, the mixing region develops a uniform green hue indicating mixing of the blue and yellow streams (Fig. 4E; "ACOUSTIC ON"). In parallel, the focusing region transitions from a sparse distribution of otherwise invisible microspheres to a well-defined particle streamline (Fig. 4F "ACOUSTIC ON").

Results from this linear integrated device (Fig. 4) establish that mixing and focusing can operate in concert under a unified piezoelectric actuation. A natural extension of this concept exploits the volumetric design freedom unique to additive manufacturing. A device with a folded channel architecture demonstrates this concept in which flow routes out of plane, traverses a curved mixing region, and returns to a downstream focusing section all within a compact footprint compatible with single-use, disposable operation (Fig. 5A and B).

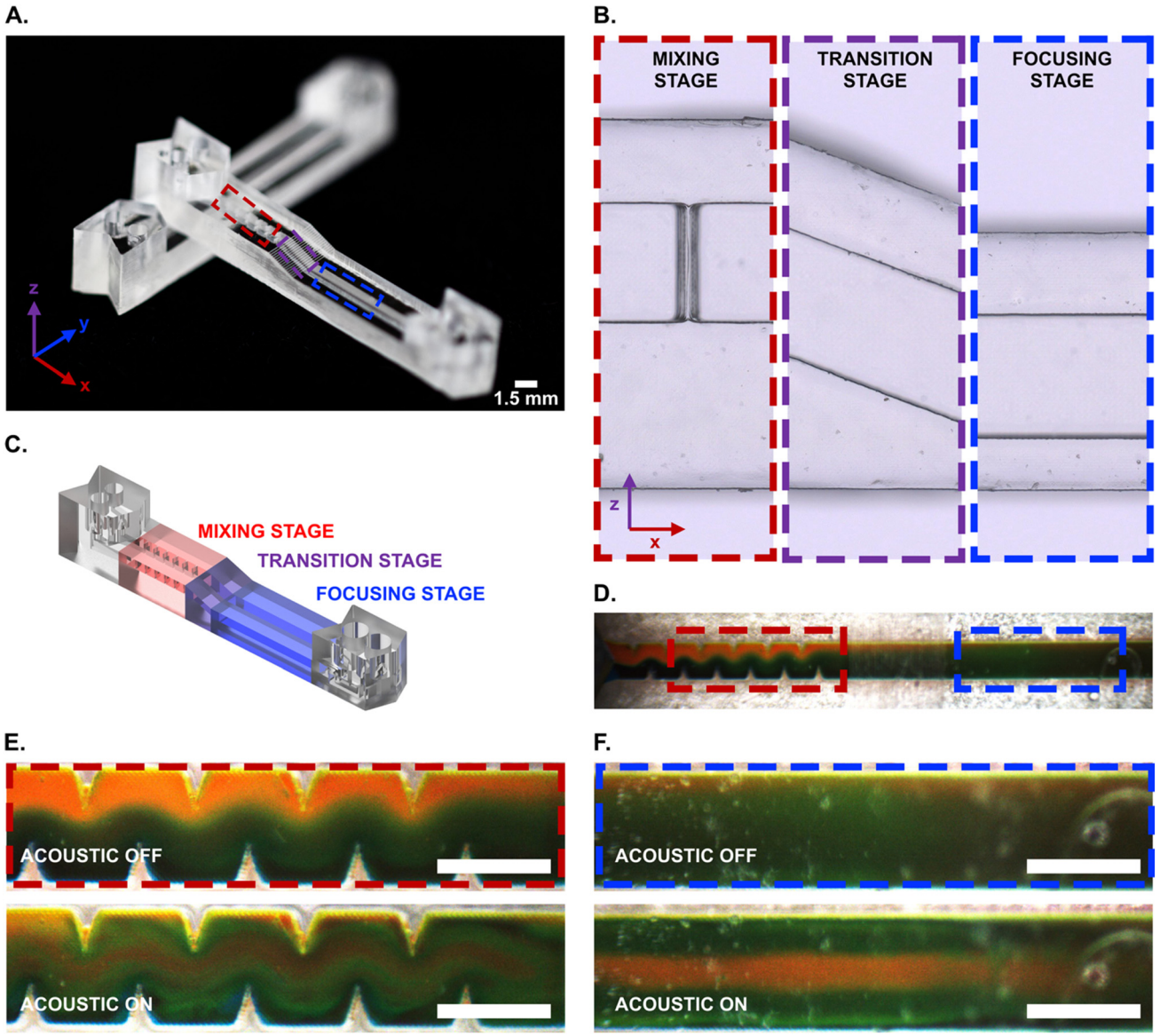

Fig. 4 (A) Photograph of an integrated acoustic mixing and focusing device, 3D-printed in resin, with three stages: mixing (red), transition (purple), and focusing (blue). (B) Side-view schematic of the device showing the three stages and varying bottom (t_{bottom}) thicknesses. (C) 3D rendering of the integrated acoustic mixing and focusing device, with the different stages indicated by distinct colors. (D) Orange fluorescent polymer microspheres suspended in fluorescein salt solution and blue-dyed DI water co-flowed through the device. (E) Mixing region imaged with acoustics off and on. Acoustic activation caused the both fluids to mix, producing green fluid with scattered orange microspheres. Scale bars represent 750 μm. (F) Focusing region imaged with acoustics off and on. Acoustic activation aggregated the orange microspheres at the channel center, forming a single streamline. Scale bars represent 750 μm.

Central to this design is a curved mixing channel (radius of curvature of 5.5 mm) dimensioned to maintain laminar flow while providing sufficient path length for complete homogenization. A return loop directs the mixed effluent to a focusing channel positioned beneath the mixing section. This stacked topology would require multiple lithographic layers, precise alignment, and sequential bonding steps if fabricated *via* conventional methods but forms here monolithically from *via* a single print. A structural air gap separates the two functional regions. The large acoustic impedance mismatch at the resin–air interface reflects incident waves and thereby isolates the resonant modes of each section permitting independent tuning of mixing and focusing performance without geometric compromise. Smoothly graded wall thicknesses varying continuously rather than in discrete laminated steps further tailor local acoustic boundary conditions, which in turn exemplifies a class of geometric feature native to additive processes.

In the absence of acoustic excitation, the coflowing streams exhibit the expected laminar stratification with interfacial mixing limited to diffusion (Fig. 5C, "ACOUSTIC OFF"). Activation of the piezoelectric element induces vigorous streaming along the curved channel yielding a uniform fluorescent signal indicative of complete mixing (Fig. 5C,

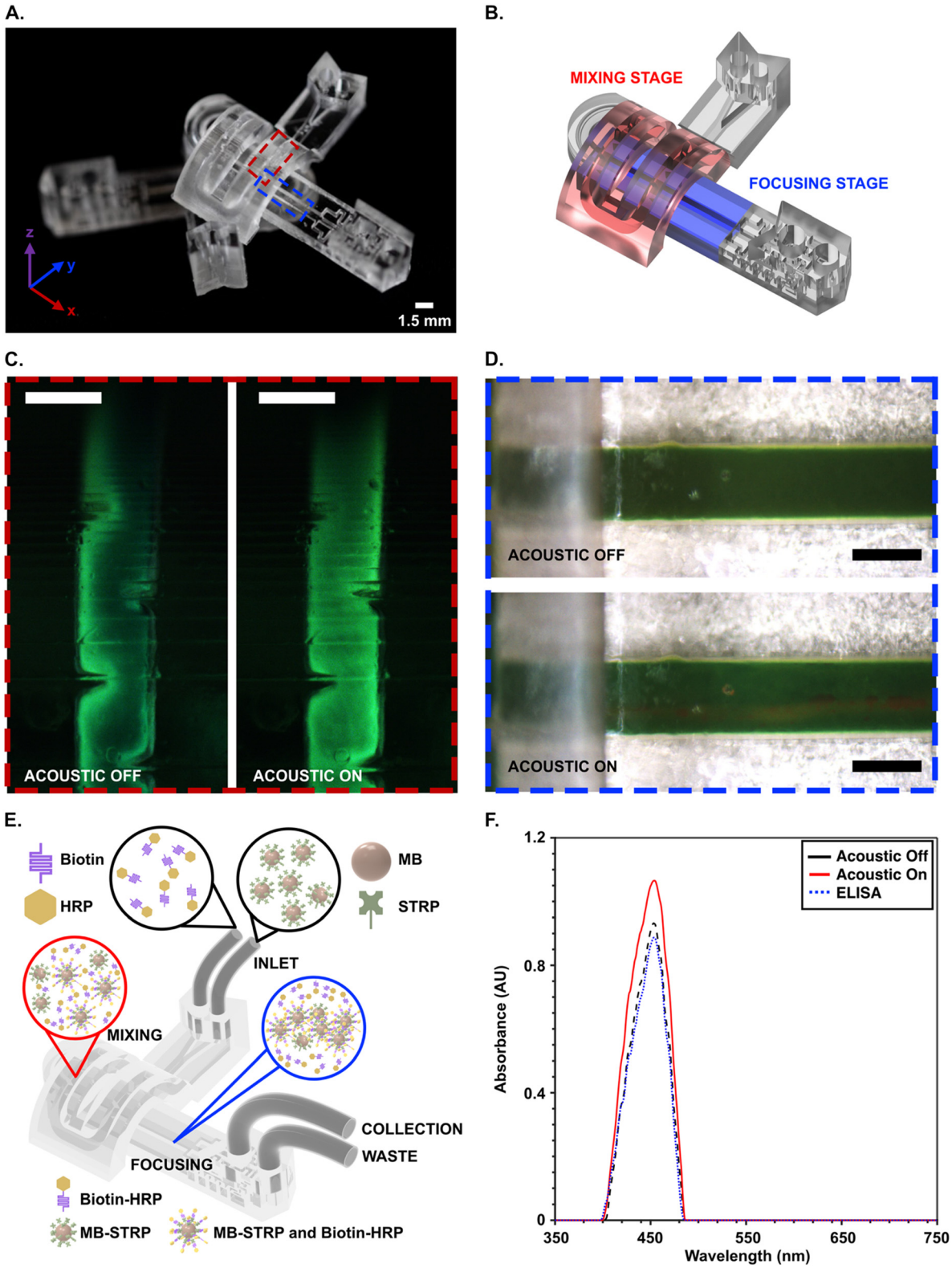

Fig. 5 (A) Photograph of an additional integrated mixing and focusing device fabricated *via* resin-based 3D printing, comprising two stages: (B) a mixing stage (red) and a focusing stage (blue). (C) Fluorescence images of the mixing region with acoustics off and on. Upon acoustic activation, the two fluids mix, resulting in a uniform green fluorescence signal. Scale bars represent 750 μm. (D) Brightfield images of the focusing region with acoustics off and on. Acoustic activation aggregates the orange microspheres at the channel center, forming a single focused streamline. (E) Schematic illustration of the enzyme-linked affinity assay and device platform. HRP is horseradish peroxidase, MB is magnetic bead, and STRP is streptavidin. (F) Absorbance measurements comparing standard process (ELISA), device performance in absence (acoustic off) and presence (acoustic on; 20 V_{pp}) of acoustophoretic mixing/focusing. Increasing absorbance is proportional to increasing concentration. Scale bars represent 750 μm.

"ACOUSTIC ON"). In the downstream focusing section the suspended particles, which are initially dispersed across the channel cross-section, migrate rapidly to the central pressure node to form a tight streamline (Fig. 5D).

To assess functional relevance of this device streptavidin-functionalized magnetic beads (MB-STRP) and biotinylated horseradish peroxidase (Biotin-HRP) were co-introduced as a model bead-based capture system. UV-vis absorbance of the processed output (Fig. 5E and F) reveals substantially elevated capture efficiency under acoustic activation. This is attributed as a direct consequence of enhanced bead–target collision frequency in the mixing zone followed by concentration of the receptor-analyte complex for downstream collection. This assay configuration mirrors the unit operations central to biomanufacturing workflows such as the affinity capture of therapeutic proteins, magnetic isolation of extracellular vesicles, and immunomagnetic selection of cells for autologous therapies. The capacity to realize such integrated, geometrically complex cartridges through rapid, iterative additive fabrication offers a route toward distributed, application-specific production platforms aligned with emerging models of personalized medicine and continuous bioprocessing.

The capability to precisely spatially engineer device and channel geometries with high precision demonstrates the versatility of 3D printing in creating complex, sophisticated acoustofluidic device architectures. By consolidating mixing and focusing in a single platform, the prototype integrated device illustrates how rational design of channel geometry and piezoelectric actuation can yield compact, multifunctional, high-performance microfluidic systems. This is a unique capability not possible in conventional glass capillary or micromachined acoustofluidic platforms.

Conclusions

These studies introduce a new class of resin-based, 3D-printed acoustofluidic devices that leverage the design freedom of additive manufacturing to enable fully integrated and multifunctional acoustic platforms. Our experimental results show that careful tuning of device geometries—particularly the thickness of polymer layers above and below the fluidic channels—surmounts the intrinsic challenges posed by low-acoustic-impedance materials. In doing so, we demonstrate robust acoustofluidic functionality for both micromixing and single-node particle focusing, facilitated by half-wavelength resonance modes in entirely 3D-printed structures.

By exploiting rapid prototyping capabilities and the capacity for true three-dimensional device architectures, this approach expands the design space for acoustofluidic systems well beyond the constraints of traditional glass- and silicon-based microfabrication methods. The integrated, single-piezo device reported here exemplifies how convergent fluid operations—mixing and focusing—can be unified in a compact, low-cost, and scalable format, thereby defining a blueprint for next-generation lab-on-a-chip technologies. We anticipate that the fundamental insights and versatile design strategies outlined in this work will catalyze further development of acoustophoretic systems for applications such as point-of-care diagnostics with 3D printing serving as a key enabler of producing high-performance, customizable, and widely accessible acoustofluidic devices.

Author contributions

Conceptualization (R. K. B., J. W. Y., T. R. R.); data curation (R. K. B.); formal analysis (R. K. B., J. W. Y., K. J., O. A.); funding acquisition (T. R. R.); investigation (R. K. B., J. W. Y., J. D.); methodology (R. K. B., J. W. Y., T. R. R.); supervision (T. R. R.); visualization (R. K. B., T. R. R.); writing – original draft (R. K. B., T. R. R.); writing – review & editing (R. K. B., J. W. Y., K. J., O. A., T. R. R.).

Conflicts of interest

The authors declare the following competing financial interest(s): T. R. R. and R. K. B. are inventors on patents and patent applications related to acoustophoretic focusing.

Data availability

The authors declare that the data supporting the findings of this study are available either within the paper or supplementary information (SI).

Supplementary information is available. See DOI: https://doi.org/10.1039/d6lc00107f.

Acknowledgements

This work was partially supported by the National Science Foundation under grants CMMI 2240170 (T. R. R.) and OIA 2229784 (T. R. R.); the Air Force Office of Scientific Research under Grant Numbers W911NF-23-1-0162 (T. R. R.) and W911NF-24-10278 (T. R. R.); and the National Institutes of Health under NIGMS grant 5P20GM113134-07 and 5P20GM113134-07S1 (T. R. R., O. A.) and T34GM141986 (J. D.). This work was also supported by a NASA Space Technology Graduate Research Opportunity (R. K. B., T. R. R.). The views and conclusions contained in this document are those of the authors and should not be interpreted as representing the official policies, either expressed or implied, of the Air Force Office of Scientific Research or the U.S. Government. We thank Prof. Charles Henry and Dr. Thaisa Baldo for helpful comments regarding the assay component of this work.

References

1 S. Zhu, F. Jiang, Y. Han, N. Xiang and Z. Ni, *Analyst*, 2020, **145**, 7103–7124.
2 Y. Yang, Y. Chen, H. Tang, N. Zong and X. Jiang, *Small Methods*, 2020, **4**, 1900451.
3 Y. Zhou, Y. Wu, L. Ding, X. Huang and Y. Xiong, *TrAC, Trends Anal. Chem.*, 2021, **145**, 116452.

4 H. Bruus, *Lab Chip*, 2011, **11**, 3742.
5 M. Wu, A. Ozcelik, J. Rufo, Z. Wang, R. Fang and T. Jun Huang, *Microsyst. Nanoeng.*, 2019, **5**, 32.
6 R. R. Collino, T. R. Ray, R. C. Fleming, C. H. Sasaki, H. Haj-Hariri and M. R. Begley, *Extreme Mech. Lett.*, 2015, **5**, 37–46.
7 R. R. Collino, T. R. Ray, L. M. Friedrich, J. D. Cornell, C. D. Meinhart and M. R. Begley, *Mater. Res. Lett.*, 2018, **6**, 191–198.
8 Y. Chen, M. Wu, L. Ren, J. Liu, P. H. Whitley, L. Wang and T. J. Huang, *Lab Chip*, 2016, **16**, 3466–3472.
9 J. Rufo, F. Cai, J. Friend, M. Wiklund and T. J. Huang, *Nat. Rev. Methods Primers*, 2022, **2**, 30.
10 T. Laurell, F. Petersson and A. Nilsson, *Chem. Soc. Rev.*, 2007, **36**, 492–506.
11 J. Park, J. Kim, S. Pané, B. J. Nelson and H. Choi, *Adv. Healthcare Mater.*, 2021, **10**, 2001096.
12 H. Xiao, M. Aliabouzar and M. L. Fabiilli, *J. Controlled Release*, 2024, **374**, 205–218.
13 J. Xu, H. Cai, Z. Wu, X. Li, C. Tian, Z. Ao, V. C. Niu, X. Xiao, L. Jiang, M. Khodoun, M. Rothenberg, K. Mackie, J. Chen, L. P. Lee and F. Guo, *Nat. Commun.*, 2023, **14**, 869.
14 D. S. Melchert, R. R. Collino, T. R. Ray, N. D. Dolinski, L. Friedrich, M. R. Begley and D. S. Gianola, *Adv. Mater. Technol.*, 2019, **4**, 1900586.
15 K. Johnson, D. Melchert, D. S. Gianola, M. Begley and T. R. Ray, *MRS Adv.*, 2021, **6**, 636–643.
16 K. E. Johnson, B. C. Montano, K. J. Nambu, E. N. Armstrong, C. L. Cobb and M. R. Begley, *Mater. Des.*, 2023, **234**, 112328.
17 S. Noparast, F. Guevara Vasquez, M. Francoeur and B. Raeymaekers, *Adv. Mater. Technol.*, 2024, **9**, 2301950.
18 M. P. Nair, A. J. T. Teo and K. H. H. Li, *Micromachines*, 2021, **13**, 24.
19 M.-S. Scholz, B. W. Drinkwater and R. S. Trask, *Ultrasonics*, 2014, **54**, 1015–1019.
20 H. Yingbin, *Mater. Horiz.*, 2021, **8**, 885–911.
21 S. Safaee, M. Schock, E. B. Joyee, Y. Pan and R. K. Chen, *Addit. Manuf.*, 2022, **51**, 102642.
22 M. Wiklund, R. Green and M. Ohlin, *Lab Chip*, 2012, **12**, 2438.
23 S. S. Sadhal, *Lab Chip*, 2012, **12**, 2292.
24 N. Nama, P.-H. Huang, T. J. Huang and F. Costanzo, *Biomicrofluidics*, 2016, **10**, 024124.
25 A. A. Doinikov, M. S. Gerlt, A. Pavlic and J. Dual, *Microfluid. Nanofluid.*, 2020, **24**, 32.
26 X. Zhao, H. Chen, Y. Xiao, J. Zhang, Y. Qiu, J. Wei and N. Hao, *Chem. Eng. J.*, 2022, **447**, 137547.
27 Z. Chen, P. Liu, X. Zhao, L. Huang, Y. Xiao, Y. Zhang, J. Zhang and N. Hao, *Appl. Mater. Today*, 2021, **25**, 101239.
28 P.-H. Huang, Y. Xie, D. Ahmed, J. Rufo, N. Nama, Y. Chen, C. Y. Chan and T. J. Huang, *Lab Chip*, 2013, **13**, 3847.
29 C. Zhang, X. Guo, P. Brunet, M. Costalonga and L. Royon, *Microfluid. Nanofluid.*, 2019, **23**, 104.
30 S. Liu, Y. Yang, Z. Ni, X. Guo, L. Luo, J. Tu, D. Zhang and J. Zhang, *Sensors*, 2017, **17**, 1664.
31 Z. Liu, Y.-J. Kim, H. Wang and A. Han, *J. Acoust. Soc. Am.*, 2016, **139**, 332–349.
32 S. M. Hagsäter, A. Lenshof, P. Skafte-Pedersen, J. P. Kutter, T. Laurell and H. Bruus, *Lab Chip*, 2008, **8**, 1178.
33 H. Bruus, *Lab Chip*, 2012, **12**, 1014.
34 T. Laurell, F. Petersson and A. Nilsson, *Chem. Soc. Rev.*, 2007, **36**, 492–506.
35 A. Lenshof, C. Magnusson and T. Laurell, *Lab Chip*, 2012, **12**, 1210.
36 I. Leibacher, P. Reichert and J. Dual, *Lab Chip*, 2015, **15**, 2896–2905.
37 T. Laurell, F. Petersson and A. Nilsson, *Chem. Soc. Rev.*, 2007, **36**, 492–506.
38 P. P. A. Suthanthiraraj, M. E. Piyasena, T. A. Woods, M. A. Naivar, G. P. López and S. W. Graves, *Methods*, 2012, **57**, 259–271.
39 C. W. Shields Iv, D. F. Cruz, K. A. Ohiri, B. B. Yellen and G. P. Lopez, *J. Visualized Exp.*, 2016, 53861.
40 A. Fornell, T. Baasch, C. Johannesson, J. Nilsson and M. Tenje, *J. Phys. D: Appl. Phys.*, 2021, **54**, 355401.
41 B. Hammarström, M. Evander, H. Barbeau, M. Bruzelius, J. Larsson, T. Laurell and J. Nilsson, *Lab Chip*, 2010, **10**, 2251.
42 G. Liu, J. Lei, F. Cheng, K. Li, X. Ji, Z. Huang and Z. Guo, *Micromachines*, 2021, **12**, 876.
43 F. Lickert, M. Ohlin, H. Bruus and P. Ohlsson, *J. Acoust. Soc. Am.*, 2021, **149**, 4281–4291.
44 I. González, L. J. Fernández, T. E. Gómez, J. Berganzo, J. L. Soto and A. Carrato, *Sens. Actuators, B*, 2010, **144**, 310–317.
45 X. Shu, H. Liu, Y. Zhu, B. Cai, Y. Jin, Y. Wei, F. Zhou, W. Liu and S. Guo, *Microfluid. Nanofluid.*, 2018, **22**, 32.
46 H. N. Açıkgöz, A. Karaman, M. A. Şahin, Ö. R. Çaylan, G. C. Büke, E. Yıldırım, İ. C. Eroğlu, A. E. Erson-Bensan, B. Çetin and M. B. Özer, Assessment of silicon, glass, FR4, PDMS and PMMA as a chip material for acoustic particle/cell manipulation in microfluidics, *Ultrasonics*, 2023, **129**, 106911.
47 C.-H. Wu, H. J. H. Ma, P. Baessler, R. K. Balanay and T. R. Ray, *Sci. Adv.*, 2023, **9**, eadg4272.
48 P. Azizian, J. Casals-Terré, J. Ricart and J. M. Cabot, *Microsyst. Nanoeng.*, 2023, **9**, 91.
49 A. Tahmasebipour, L. Friedrich, M. Begley, H. Bruus and C. Meinhart, *J. Acoust. Soc. Am.*, 2020, **148**, 359–373.
50 A. Ozcelik, *Actuators*, 2022, **11**, 249.
51 G. Cai, L. Xue, H. Zhang and J. Lin, *Micromachines*, 2017, **8**, 274.
52 Z. Li, B. Zhang, D. Dang, X. Yang, W. Yang and W. Liang, *Sens. Actuators, A*, 2022, **344**, 113757.
53 N. Nama, P. H. Huang, T. J. Huang and F. Costanzo, *Biomicrofluidics*, 2016, **10**, 024124.
54 Z. Chen, P. Liu, X. Zhao, L. Huang, Y. Xiao, Y. Zhang, J. Zhang and N. Hao, *Appl. Mater. Today*, 2021, **25**, 101239.
55 M. B. Özer and B. Çetin, *J. Acoust. Soc. Am.*, 2021, **149**, 2802–2812.
56 F. Lickert, M. Ohlin, H. Bruus and P. Ohlsson, *J. Acoust. Soc. Am.*, 2021, **149**, 4281–4291.
57 C. Zhang, P. Brunet, L. Royon and X. Guo, *Chem. Eng. J.*, 2021, **410**, 128252.
58 A. Lenshof, M. Evander, T. Laurell and J. Nilsson, *Lab Chip*, 2012, **12**, 684.